Ptychographic inversion via Wigner distribution deconvolution: Noise suppression and probe design

Peng Li *, Tega B. Edo, John M. Rodenburg

Department of Electrical and Electronic Engineering, University of Sheffield, S1 3JD, UK

ABSTRACT

We reconsider the closed form solution of the ptychographic phase problem called the Wigner Distribution Deconvolution Method (WDDM), which has remained discarded for twenty years. Ptychographic reconstruction is nowadays always undertaken by iterative algorithms. WDDM gives rise to a 4 dimensional data cube of all the relative phases between points in the diffraction plane. Here we demonstrate a novel method to use all this information, instead of just the small subset used in the original 'stepping out' procedure developed in the 1990s, thus greatly suppressing noise. We further develop a method for designing an improved probe (illumination function) to further decrease noise effects during the deconvolution division. Combining these two with an iterative procedure for the deconvolution, which avoids the usual difficulty of a divide by a small number, we show in model calculations that WDDM competes well with the modern conventional iterative methods like ePIE (the extended Ptychographical Iterative Engine).

© 2014 Elsevier B.V. All rights reserved.

1. Introduction

The concept of ptychography was proposed by Walter Hoppe [1–5] as a way to solve the phase problem in crystallography by using coherent interference between adjacent reflections, combined with some variation (diversity) in the illumination (often called the probe), such as (most simply) moving it laterally. It was not until 1989 before a practical computational method for using this type of information, called the Wigner distribution deconvolution method (WDDM), was proposed [6,7,11]. The deconvolution process in WDDM is remarkable in that (1) it solves a highly nonlinear problem (the phase problem) with linear computations, and (2) it can remove the effect of using complicated forms of illumination incident upon the specimen. The source of the phase information comes from the fact that many diffraction patterns are sequentially recorded from an array of illumination points on the specimen. As the illumination (or object) is scanned across these points, the intensity of each pixel in the diffraction pattern varies. A key step in WDDM is that (amongst other things) a Fourier transform of these variations is taken with respect to the illumination position, and it is this that filters out the phase differences between different areas of the diffraction pattern. The success of this algorithm was experimentally demonstrated with optical light

[7], x-rays [8] and, using a smaller subset of the data, with electrons [9].

However, there were quite a few problems with WDDM. The first was the number of data required: to achieve the deconvolution, the illumination must be moved over a grid of positions separated by the desired resolution in the final reconstruction. At each of these positions, an entire diffraction pattern must be recorded, giving rise to a very large four-dimensional (4D) set of data. Given the cost of computing random access memory in the early 1990s, it is no surprise that the largest field of view that could be practically calculated then was just 32×32 pixels: not very impressive. Secondly, the deconvolution step was often ill-conditioned in ways that were unpredictable, although clearly dependent on the form of the illumination function. Finally, that there was no obvious way of using all the data. After the deconvolution step, we are left with a 4D cube of data representing the complex product (and hence phase) between every point in the diffraction pattern and the complex conjugate of every other point in the diffraction pattern. That is, in the language of electron microscopy, the phase difference between all pairs of diffracted beams. When the object is non-crystalline, thousands (or even millions) of pixels can be measured in the diffraction pattern, meaning that tens of billions of phase differences can, in principle, be ascertained. Of course, the actual object will only contain a much smaller number of pixels over the field of view. The historical approach used to condense these data was an inelegant process called stepping out, which only used a fraction of the data

available. Because of all these various issues, WDDM failed to reliably yield acceptable high-quality reconstructions.

In this paper, we first propose and demonstrate a reliable projection strategy to implement the stepping out in reciprocal space in a very comprehensive way, using all the measured data. We then consider the deconvolution step of the algorithm and demonstrate a means of generating an improved probe for WDDM: i.e. we engineer a field of illumination which encodes the recorded data so that the deconvolution is very well conditioned. Finally, we introduce an iterative variation in the deconvolution process which, when combined with the former developments, greatly suppresses noise. We show that this is more robust to noise than the commonly employed PIE algorithm (that is, the extended Ptychographical Iterative Engine – ePIE [10] – run on the assumption that the illumination function is known). The organisation of this paper is as follows: for completeness Section 2 rehearses a complete derivation of WDDM; Section 3 introduces the new projection strategy; Section 4 describes a method for designing an improved illumination function and also an iterative strategy for further suppressing noise in the algorithm; Section 5 demonstrates the theory with simulations; conclusions are presented in Section 6.

2. Derivation of WDDM

Here we keep all the nomenclature from Rodenburg and Bates [11]. The recorded intensity dataset can be described as follows:

$$|M(r',\rho)|^2 = \mathcal{F}_r[a(r-\rho)\psi(r)] \times \{\mathcal{F}_r[a(r-\rho)\psi(r)]\}^*$$
$$= \iint a(r_1-\rho)a^*(r_2-\rho)\psi(r_1)\psi^*(r_2)e^{i2\pi r'(r_1-r_2)}dr_1 dr_2, \quad (1)$$

where r', r and ρ respectively represent the coordinates of the detector plane, the specimen plane and the probe scan position in the specimen plane (see Fig. 1). a and ψ represent the probe and specimen functions respectively, and $*$ denotes the complex conjugate. In the earlier work of the Cambridge group [9], ψ was described as the exit wave that would emanate from a thin specimen if it were illuminated by plane wave (hence the wave function nomenclature, ψ). Since then it has been recognised that it is better to regard ψ as a complex transfer function (unity representing free space): this is especially clear when multiple layers of the object are solved for using 3D scattering versions of ptychography [12]. Under these circumstances, none of the layers of specimen have any direct relationship to an exit wave, either when the illumination is at any one position, or if the object was illuminated by a plane wave. r_1 and r_2 are the dummy variables of

Fig. 1. Definition of the coordinates. The specimen and the scan position (r and ρ) share the same coordiante in the specimen plane.

the integration. $\mathcal{F}_r[*]$ corresponds to a Fourier transform along r and is defined by

$$\mathcal{F}_r[g(r)] = \int g(r)e^{i2\pi rr'}\, dr. \quad (2)$$

Note that, following the earlier literature, the forward transform is defined here as having a positive exponential.

The key mathematic step in WDDM is to take an inverse Fourier transform $(\mathcal{F}^{-1})$ of the dataset along r' and a Fourier transform along ρ, such that

$$H(r,\rho') = \mathcal{F}_{r'}^{-1}\mathcal{F}_\rho[|M(r',\rho)|^2]$$
$$= \iint a(r_2+r-\rho)a^*(r_2-\rho)\psi(r_2+r)\psi^*(r_2)e^{i2\pi\rho\rho'}\, dr_2\, d\rho. \quad (3)$$

Using variable substitution $t = r_2 - \rho$ in Eq. (3), we get

$$H(r,\rho') = \int\int a(t+r)a^*(t)\psi(r_2+r)\psi^*(r_2)e^{i2\pi(r_2-t)\rho'}\, dr_2\, dt$$
$$= \int a(t+r)a^*(t)e^{-i2\pi t\rho'}\, dt \int \psi(r_2+r)\psi^*(r_2)e^{i2\pi r_2\rho'}\, dr_2. \quad (4)$$

It should be noted that the separation of the two integrations in Eq. (4) depends upon ρ being a cyclic coordinate, because otherwise r_2 affects the start or the end of the integration over t (t is just a shifted coordinate of ρ). However, in a real experiment the probe position coordinate ρ is linear. The strategy used to make this separation possible for a real ptychography dataset is to make the dataset generated from a linear scan the same as that generated from a circular scan. The only discrepancy in the results generated with these scanning regimes occurs at the edge of the scan. In the circular scanning regime, parts of probe that are out of the edge of specimen wrap around to the opposite side of the specimen. This is equivalent to a linear scan with a periodic specimen (see Fig. 2). Therefore, if the sum of the support sizes of the probe (S_p) and the specimen (S_s) is smaller than the calculation window size S, then a circular scan has the same results as a linear scan. The separable condition becomes

$$S_p + S_s \leq S. \quad (5)$$

This requirement applies to both the Cartesian coordinates of r. Note that since the diffraction plane and the specimen plane are related by a Fourier transform, which is implemented here using FFT, the relation between the pixel size in diffraction plane Δu and the pixel size in specimen plane Δx (which is equal to the step size) is defined by

$$\Delta x = \frac{\lambda L}{N\Delta u}, \quad (6)$$

where λ, L and N are the wave length, camera length (distance from the detector to the specimen) and number of the detector pixels respectively.

Now for any general function $q(r)$ we can define a quantity

$$\chi_q(a,b) = \int q(c+a)q^*(c)e^{i2\pi cb}\, dc, \quad (7)$$

which is called the Wigner distribution function [13]. This definition allows us to rewrite Eq. (4) in the compact form

$$H(r,\rho') = \chi_a(r,-\rho')\chi_\psi(r,\rho'). \quad (8)$$

The advantage of forming $H(r,\rho')$ becomes obvious because it makes the probe and the specimen separable, which means we can separate out the influences of all the aberrations of the illumination to get a high resolution image. We can form $\chi_\psi(r,\rho')$ by dividing every point in $H(r,\rho')$ by $\chi_a(r,-\rho')$. This is identical to a conventional deconvolution process. To avoid the division by zero, we use the Wiener filter [14], that is

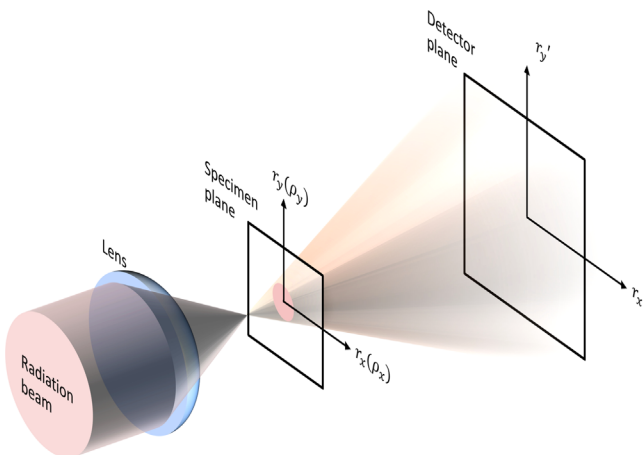$$\chi_\psi(r,\rho') = \chi_a^*(r,-\rho')H(r,\rho')/(|\chi_a(r,-\rho')|^2+\epsilon), \quad (9)$$
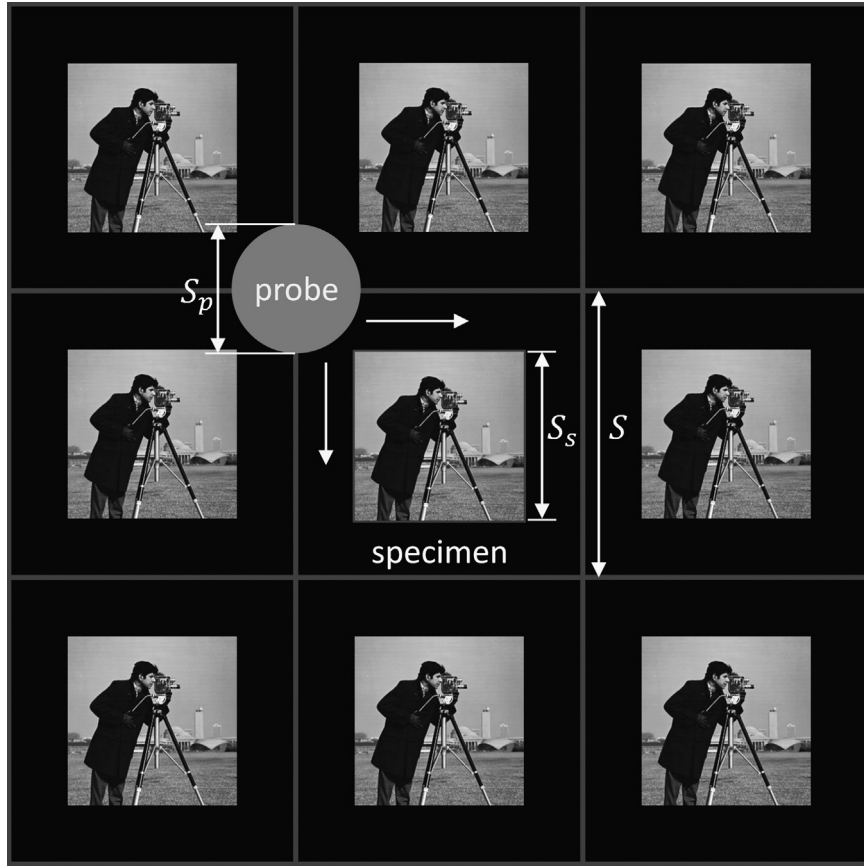
Fig. 2. Illustration of the connection between a circular and a linear scan, using a periodic specimen. The transmission coefficient of the dark margin is zero. The white arrows indicate the scanning directions.

where ϵ is some small constant. However, $\chi_\psi(r,\rho')$ is still constrained by the support region (non-zero region) of $\chi_a(r,-\rho')$. Therefore, to process $\chi_\psi(r,\rho')$ we need to know the support region of $\chi_a(r,-\rho')$.

Suppose the probe has a support size of r_{max} in real space and ρ'_{max} in reciprocal space. The definition of $\chi_a(r,-\rho')$ in Eq. (7) implies that $\chi_a(r,-\rho')$ has a support size of $2r_{max}$ along r. To better understand the support size along ρ', we change the form of $\chi_a(r,-\rho')$ to

$$\chi_a(r,-\rho') = \int A(r')A^*(r'+\rho')e^{-i2\pi rr'}\,dr', \qquad (10)$$

where A is the Fourier transform of a. Eq. (10) implies that $\chi_a(r,-\rho')$ has a support size of $2\rho'_{max}$ along ρ'. If either r_{max} or ρ'_{max} is smaller than the half of the calculation window size, $\chi_a(r,-\rho')$ is constrained along the corresponding direction. To reconstruct the specimen image after the deconvolution, we need to implement another Fourier transform on $\chi_\psi(r,\rho')$ either along r or along ρ' depending on the constraints of $\chi_a(r,-\rho')$. If the constraint is along ρ', we implement the Fourier transform along r as follows:

$$D(r',\rho') = \mathcal{F}_r[\chi_\psi(r,\rho')]$$
$$= \Psi(r')\Psi^*(r'-\rho'), \qquad (11)$$

where $\Psi(r')$ is the Fourier transform of the specimen function $\psi(r)$. If the constraint is along r, we implement the inverse Fourier transform along ρ' as follows:

$$L(r,\rho) = \mathcal{F}_{\rho'}^{-1}[\chi_\psi(r,\rho')]$$
$$= \psi(\rho+r)\psi^*(\rho). \qquad (12)$$

Eq. (11) is always the case we apply when the probe is formed by a lens with a sharp aperture at the back focal plane (this translates directly into a sharp cut-off along ρ'). In the case of electron microscopy, the cut-off is softer, caused by partial incoherence effects like instabilities in the high voltage source, the lens currents and magnetic field interference which oscillates the probe [15]. Eq. (12) applies when there is an aperture coincident with the specimen – an experimental configuration which is generally impractical. Therefore, to avoid the constraint along r for implementing the stepping out procedure, we need to make the support size of the probe in real space bigger than the half of calculation window size. According to Eq. (5), in order to obtain the biggest field of view for the specimen, the optimal combination of the support sizes of the probe S_p and the specimen S_s is $S_p = S_s = S/2$. The object and/or the probe function need not be strictly finite if a window function is employed, as demonstrated experimentally in [7].

3. Exploitation of all the phase information using a projection strategy

As mentioned above, information is constrained along ρ'. To recover high resolution information about the specimen, we need an algorithm to utilise the data lying in the r' direction (which derives from the fact that the detector is large, collecting high-angle, high-resolution information), while avoiding the constraint in the ρ' direction (the so-called ρ' cut-off), which derives from the fact that the lens which is used to form the probe has a cut-off due to its finite aperture. Rodenburg and Bates used the stepping out method [11]. Here, we present a projection method that recovers all the information as well as improving the robustness of the method to noise.

As shown in Fig. 3, the specimen's spatial frequency is cut off by the limit ($\pm\rho'_{max}$). In the stepping out method, a route that contains all the specimen frequency information is chosen, so that we can recover the lost frequency components. From left to right, first assigning an arbitrary phase to A, we can calculate A from A^*A. Then we can derive B from A^*B, C from B^*C, D from C^*D and E from D^*E. Although the stepping out method can manage to recover all the frequency components, it needs a method to choose a suitable fraction of data and cannot make use of all the available data simultaneously. In the presence of noise, if we choose a wrong data segment to start with, the error will accumulate as the stepping out progresses.

Here we improve the stepping out method by introducing a projection strategy:

$$\Psi(r') = \frac{\sum_{\rho'} \Psi(r'-\rho')D(r',\rho')}{\sum_{\rho'} |\Psi(r'-\rho')|^2}, \quad |\rho'| \le \rho'_{max}. \tag{13}$$

As we can see, the two summations in Eq. (13) are implemented along ρ', like a projection along the corresponding direction. This is why we call the method a projection strategy. Fig. 4 shows how this recovers all the information in a straightforward and more reliable way. First assigning an arbitrary phase to C and using $D^*(0,\rho')/\sqrt{D(0,0)}$, we can get $\Psi(\rho') = [0, B, C, D, 0]$, losing the two
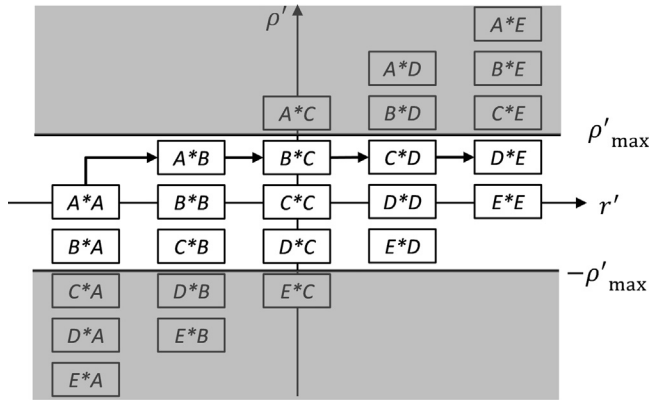

Fig. 3. Schematic representation of the dataset $D(r',\rho')$, showing how the stepping out method works. The arrow line shows one of the routes to implement the stepping out method.
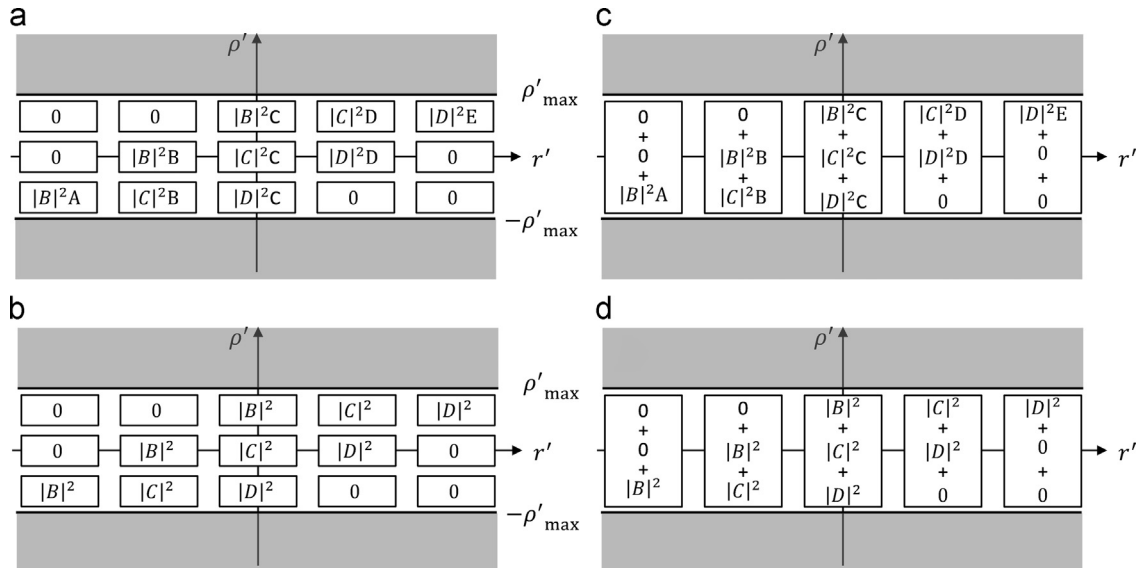
highest frequencies A and E. Then we calculate $\Psi(r'-1)D(r',1) = [0, 0, |B|^2C, |C|^2D, |D|^2E]$, $\Psi(r'-0)D(r',0) = [0, |B|^2B, |C|^2C, |D|^2D, 0]$ and $\Psi(r'+1)D(r',-1) = [|B|^2A, |C|^2B, |D|^2C, 0, 0]$. In the same way, we calculate $|\Psi(r'-1)|^2 = [0, 0, |B|^2, |C|^2, |D|^2]$, $|\Psi(r'-0)|^2 = [0, |B|^2, |C|^2, |D|^2, 0]$ and $|\Psi(r'+1)|^2 = [|B|^2, |C|^2, |D|^2, 0, 0]$. Using Eq. (13) we can solve $\Psi(r') = [A, B, C, D, E]$. Since the dataset we are processing is 4D (2D diffraction patterns with a 2D scan array) and highly redundant, the projection method improves the robustness to noise by using all the measured data in the image recovery process.

After we obtain $\Psi(r')$, we just need to apply an inverse Fourier transform to reconstruct the specimen image $\psi(r)$.

4. Noise suppression via probe improvement and an iterative method

Noise is inevitable in real experiments and imposes inconsistency in the dataset. Fortunately the projection strategy can mitigate this inconsistency by averaging all the available data along the projection direction. The main challenge however is the deconvolution process which will introduce big errors where $\chi_a(r,-\rho')$ has small values. From the deconvolution point of view, the most favourable probe to use experimentally will have an even distribution over $\chi_a(r,-\rho')$ with as few local minima as possible. The easiest way to make this kind of probe is a diffuser [16,17]. In order to improve and engineer such a probe, we have found it is possible to use an iterative method similar to a conventional ptychographic reconstruction. From the definition of $\chi_a(r,-\rho')$ in Eq. (7), we can see that the modulus of $\chi_a(r,-\rho')$ is the same as the ptychographical dataset from the setup where the specimen is the conjugate of the probe. We can therefore define the modulus of $\chi_a(r,-\rho')$ so that the deconvolution is stable (ideally a flat constant modulus) and use ePIE to solve for the probe. Although ePIE cannot converge to a solution which gives the exact $\chi_a(r,-\rho')$ we want, the method significantly spreads out the distribution of $\chi_a(r,-\rho')$.

We furthermore use an iterative method that can suppress the residual errors introduced by the deconvolution, which can never be made perfect even when we employ our improved probe. Since $\chi_\psi(r,\rho')$ is a highly redundant 4D dataset, the deconvolved data with big errors in the $\chi_\psi(r,\rho')$ function can be refined using
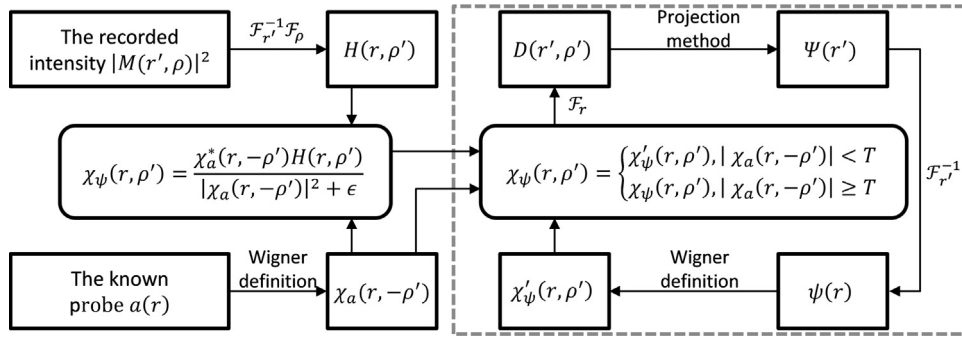

Fig. 4. Implementation of the projection strategy. First, for each ρ' we calculate (a) $\Psi(r'-\rho')D(r',\rho')$ and (b) $|\Psi(r'-\rho')|^2$. We then sum along ρ' to get (c) $\sum_{\rho'} \Psi(r'-\rho')D(r',\rho')$ and (d) $\sum_{\rho'} |\Psi(r'-\rho')|^2$ respectively. Last, the division of (c) and (d) gives all the frequencies of $\Psi(r')$.

Fig. 5. Flow chart of noise suppression WDDM. The part in the dashed square shows the noise suppression loop. The inputs are the recorded intensity $|M(r',\rho)|^2$ and the known probe $a(r)$ and the output is the specimen function $\psi(r)$.
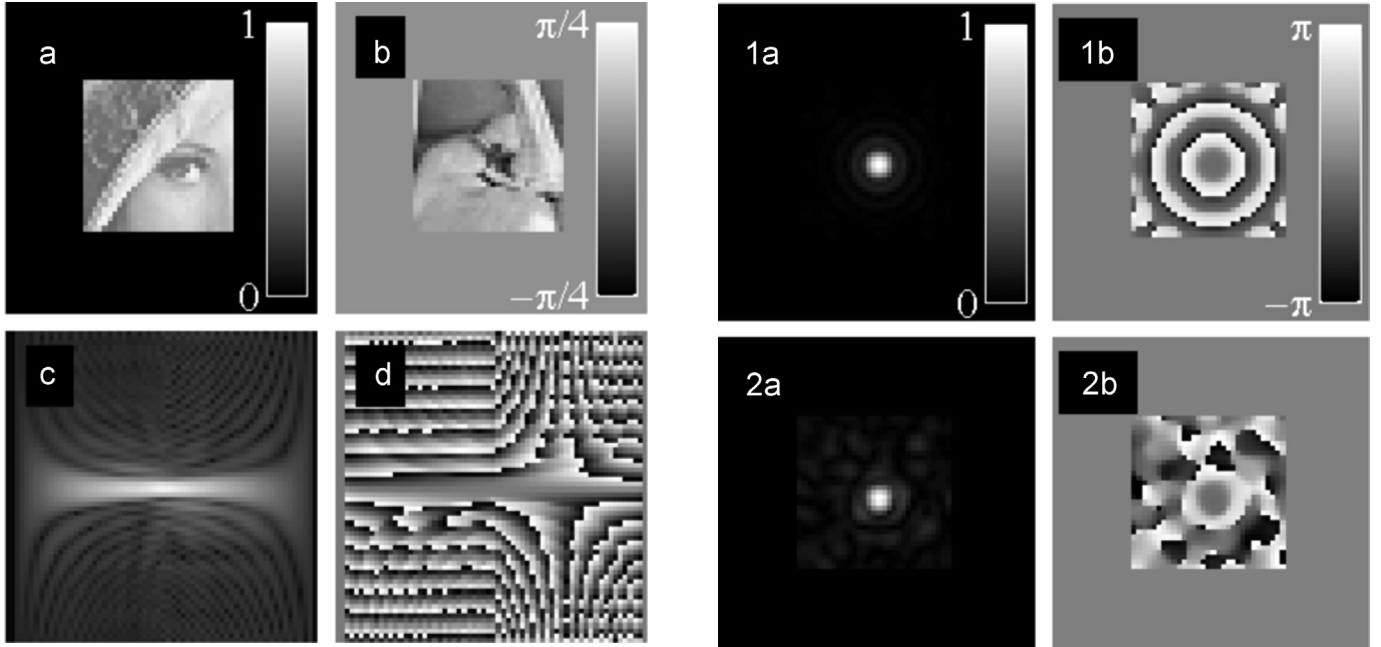

Fig. 6. The simulated specimen and its Wigner distribution. (a) The modulus and (b) the phase of the specimen. (c) The square-root of the modulus and (d) the phase of the specimen's Wigner distribution. We take the square-root to improve the display contrast.

information from areas with small errors. This fact is exploited by the noise suppression method present here. First we can reconstruct an initial image of the specimen from the non-optimally deconvolved $\chi_\psi(r,\rho')$ and generate a new $\chi'_\psi(r,\rho')$ from the initial image. We then use the values in the generated $\chi'_\psi(r,\rho')$ to replace the values in the very bad regions of the deconvolved $\chi_\psi(r,\rho')$. We undertake this replacement where the absolute values of $\chi_a(r,-\rho')$ are smaller than a pre-set threshold T. Placing these steps in a loop gives the iterative algorithm in Fig. 5. Using this algorithm, we can suppress the noise significantly and obtain acceptable reconstructions.

5. Model calculations based on three different probes

In this section, we demonstrate the success of the proposed improvements through simulations with three different probes. The specimen (including its Wigner distribution) and the probes are respectively shown in Figs. 6 and 7. They both fill up only half of the calculation window according to the optimal size combination mentioned in Section 2. Since WDDM needs to do a very dense scan, it imposes challenging requirements on both the computation and the memory of the computer. To alleviate this
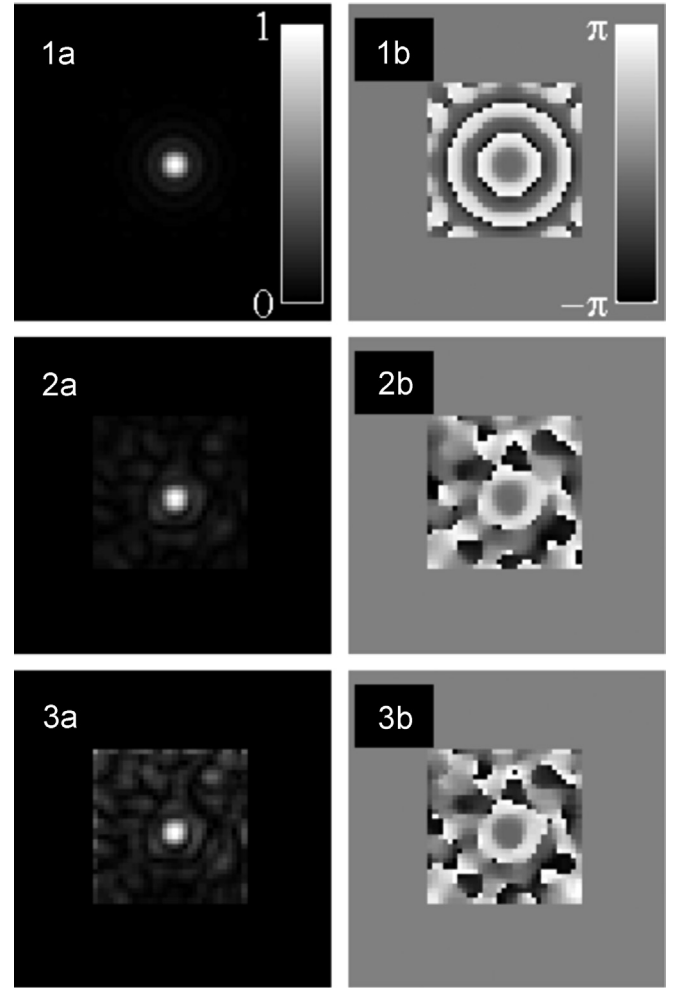

Fig. 7. The simulated probes. From (1) to (3), they are respectively the defocused probe, the diffused probe and the improved probe. (a) Represents the moduli and (b) represents the phases. The modulus bar is applied to all the modulus parts and the phase bar applied to all the phase parts.

problem, we set the probe and the object to be 64×64 pixels. The scan grid is also 64×64 with the step size of 1 pixel. These experiments utilise three different types of probes. The first probe is a defocused probe. It is generated from the configuration of the scanning transmission electron microscope (STEM): the modelled beam voltage is 100 kV, the aperture size at the back focal plane is 3 mrad and the defocus is 1000 Å. Although these parameters would not generally be suitable for high-resolution imaging (a 3 mrad aperture is relatively small), in ptychography it is

generally better to have relatively parallel illumination to maintain the projection approximation. The spherical aberration is not considered here given the small aperture size. The second probe is a diffused probe. It is generated using the same parameters as the defocused probe, except putting a phase diffuser (ranging from $-\pi/2$ to $\pi/2$) at the back focal plane. The third probe is an improved probe based on the diffused probe. It is generated from the square root of the modulus of the diffused probe's Wigner distribution by running ePIE, as described above, for 4 iterations. The specimen and probe functions are two-dimensional. Therefore, the corresponding Wigner distributions are four-dimensional. The limitations of displaying a 4D dataset on a 2D page means that, hereinafter only the y-axis part of each Wigner distribution, i.e. $\chi(r_0, r_y, \rho_0', \rho_y')$, is displayed.

To simulate the imperfections of a real experiment (such as partial coherence [11]), we manually cut out one-third of the data along ρ' in $\chi_\psi(r, \rho')$ during the reconstruction. In practice, the cut-off will often be soft, but this can be accounted for in the deconvolution process. Poisson distributed noise with total counts of 10^6 in each diffraction pattern is added to the data. Fig. 8 shows the WDDM reconstructions from these three different probes. Obviously, the defocused probe is the worst case, because most of the energy of its Wigner distribution $\chi_a(r, -\rho')$ is in the centre. As a result, the deconvolved $\chi_\psi(r, \rho')$ is inaccurate around the edges, causing very noisy specimen reconstructions. For the diffused probe, its Wigner distribution $\chi_a(r, -\rho')$ stretches out more, producing better deconvolved $\chi_\psi(r, \rho')$ and specimen reconstructions. For the improved probe, its Wigner distribution $\chi_a(r, -\rho')$ completely stretches out and fills in the whole window. As a result,

the deconvolved $\chi_\psi(r, \rho')$ is much less noisy and the corresponding specimen reconstructions are much better. The normalised mean square errors of the specimen reconstructions shown in Fig. 8 are 1.7648, 0.0257 and 0.0073 respectively. Note that all of these calculations use the projection strategy described in Section 3.

As the noise level increases, the application of the probe improvement is no longer enough to obtain acceptable reconstructions. Fortunately, the noise suppression method can considerably enhance the deconvolution performance. Four noisy datasets were simulated with total counts of 10^6, 10^5, 10^4 and 10^3 for each diffraction pattern. The noise suppression method and PIE were run over 50 iterations, and the results for each reconstruction are shown in Fig. 9. The corresponding normalised mean square errors of the specimen reconstructions are calculated and shown in Table 1. When the noise level is low (10^6 and 10^5), the defocused probe fails to produce acceptable specimen reconstructions, while both the diffused probe and the improved probe yield good specimen reconstructions with slightly bigger errors than that of PIE. However, when the noise level is increased to 10^4, reconstructions from the defocused probe, the diffused probe and PIE degrade dramatically, but the reconstructions from the improved probe are still very good. And this trend also applies for the very small counts (10^3) calculations, where both the defocused probe and the diffused probe cannot even give recognisable reconstructions whereas the improved probe calculation gives a good reconstruction. The reason the WDDM with the improved probe performs better than the PIE algorithm (when processing the very noisy datasets), is because the projection strategy can average the effect of noise over the entire data set.
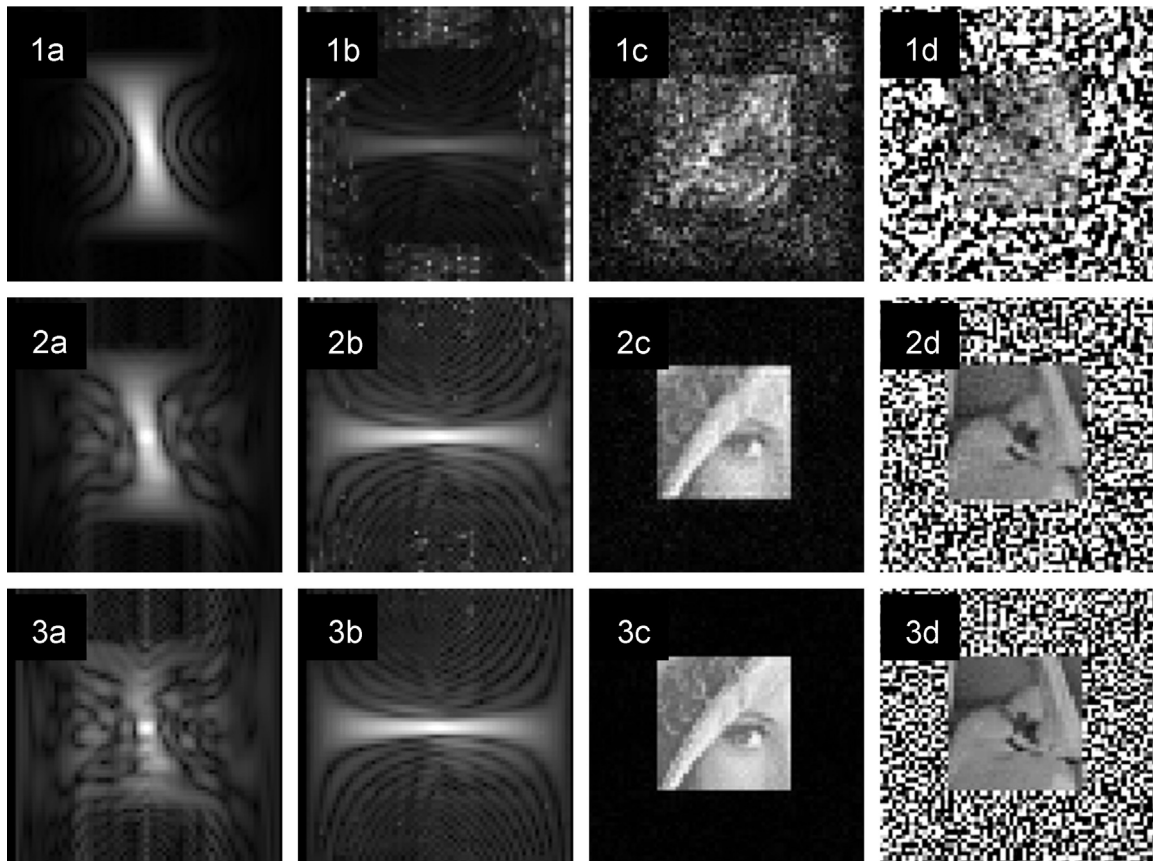

Fig. 8. Reconstructions from different probes. From (1) to (3), they respectively represent WDDM reconstructions from the defocused probe, the diffused probe and the improved probe. (a) The square root of the moduli of the probes' Wigner distributions, (b) the square root of the moduli of the specimens' deconvolved Wigner distributions, (c) the moduli and (d) the phases of the reconstructed specimens. We take the square-root to improve the display contrast.
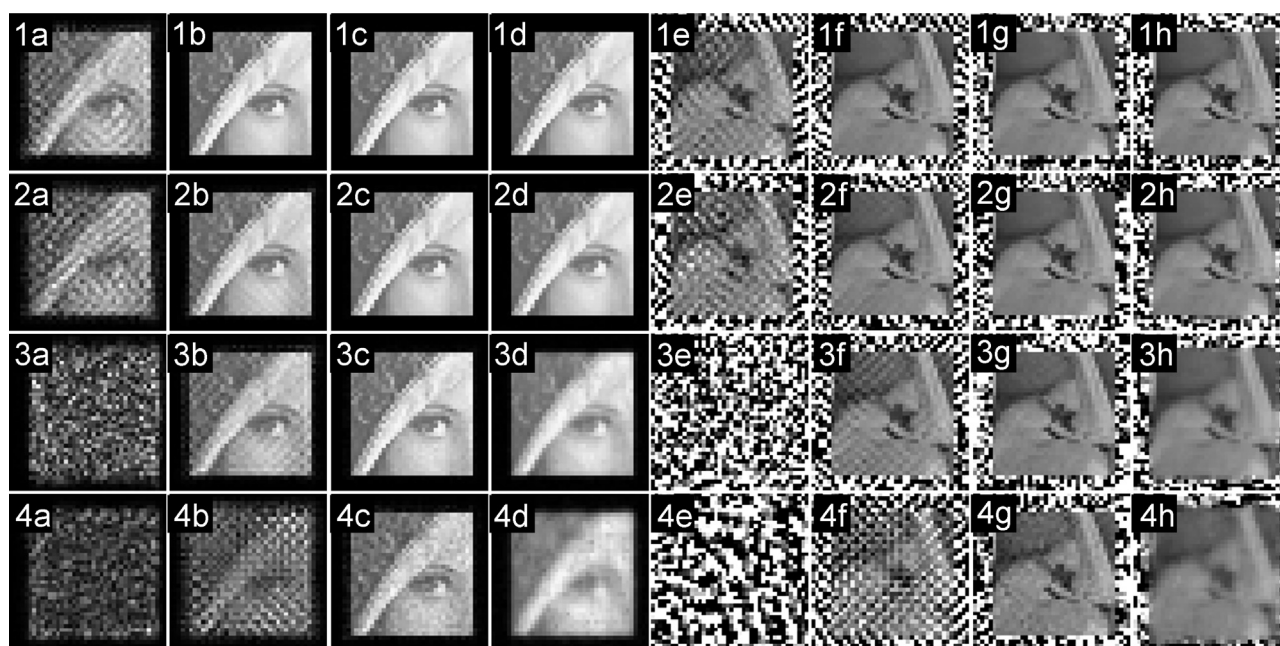
Fig. 9. Results of noise suppression WDDM and PIE from different probes with different noisy datasets. From (1) to (4), they respectively represent reconstructions from datasets with total counts of 10^6, 10^5, 10^4 and 10^3 for each diffraction pattern. (a) The moduli and (e) the phases of the reconstructed specimens from WDDM with the defocused probe. (b) The moduli and (f) the phases of the reconstructed specimens from WDDM with the diffused probe. (c) The moduli and (g) the phases of the reconstructed specimens from WDDM with the improved probe. (d) The moduli and (h) the phases of the reconstructed specimens from PIE with the improved probe. 50 iterations are implemented for both noise suppression WDDM and PIE algorithms.

Table 1

Normalised mean square errors of specimen reconstructions from datasets with different noise levels.

Noise level	WDDM defocused probe	WDDM diffused probe	WDDM improved probe	PIE improved probe
10^6	0.0464	0.0040	0.0037	0.0025
10^5	0.1160	0.0067	0.0038	0.0029
10^4	597.94	0.0247	0.0050	0.0108
10^3	73,540	0.3673	0.0150	0.0575

6. Conclusions

In this paper, we have rehearsed the derivation of WDDM and considered the conditions for which its implementation is valid. We have shown that the sum of the support sizes of the specimen and the probe should be smaller than the calculation window size to make sure that a linear scan is equivalent to a circular scan. This is essential for the Fourier transform of the intensity datasets to equal to the product of the Wigner distribution functions of the specimen and the probe, so that the influences of the probe can be separated out of the specimen by a deconvolution. The deconvolution introduces errors when noise exists and we have presented several ways to improve the performance at the different implementation stages of WDDM. Once the deconvolution step has been undertaken, we are presented with a four-dimensional data set representing all pairs of phase difference between all pixels in the diffraction plane. Unlike previous work where this has not been properly exploited, we have proposed the projection strategy which is capable of using all the measured data to mitigate inconsistencies. Meanwhile, from the deconvolution point of view, we have conjectured that a good probe for WDDM is one that has a wide Wigner distribution with broadly flat modulus, thus minimising the effects of division by small numbers. To calculate a probe necessary to achieve this condition, we set an even Wigner distribution and use its modulus as ptychographical data to generate an improved probe by running ePIE: this is possible because the form of the Wigner Distribution is analogous to the conventional ptychographic dataset. Furthermore, we have also put forward an iterative noise suppression method to enhance the performance of WDDM by exploiting the high redundancy of the dataset. The basic idea is to use the well deconvolved data to refine the badly deconvolved data. All these improvements have been successfully demonstrated via simulated results. The combination of all these improvements even enables WDDM to produce better reconstructions than the PIE algorithm with very noisy data.

Acknowledgements

References

[1] W. Hoppe, Diffraction in inhomogeneous primary wave fields. 1. Principle of phase determination from electron diffraction interference, Acta Crystallogr. A 25 (1969) 495–501.

[2] W. Hoppe, Diffraction in inhomogeneous primary wave fields. 2. Optical experiments for phase determination of lattice interferences, Acta Crystallogr. A 25 (1969) 502–507.

[3] W. Hoppe, Diffraction in inhomogeneous primary wave fields. 3. Amplitude and phase determination for nonperiodic objects, Acta Crystallogr. A 25 (1969) 508–515.

[4] R. Hegerl, W. Hoppe, Dynamische Theorie der Kristall-strukturanalyse durch Elektronenbeugung im inhomogen Primarstrahlwellenfeld, Ber. Bunsenges. Physik. Chem. 74 (1970) 1148–1154.

[5] R. Hegerl, W. Hoppe, Phase evaluation in generalized diffraction (ptychography), in: Proceedings of the Fifth European Congress Electron Microscopy, vol. 14, 1972, pp. 628–629 (Manchester).

[6] R.H.T. Bates, J.M. Rodenburg, Sub-Angstrom transmission microscopy: a Fourier transform algorithm for microdiffraction plane intensity information, Ultramicroscopy 31 (1989) 303–307.

[7] B.C. McCallum, J.M. Rodenburg, 2-Dimensional optical demonstration of Wigner phase retrieval microscopy in the STEM configuration, Ultramicroscopy 45 (1992) 371–380.

[8] H.N. Chapman, Phase-retrieval X-ray microscopy by Wigner distribution deconvolution, Ultramicroscopy 66 (1996) 153–172.

[9] J.M. Rodenburg, B.C. McCallum, P.D. Nellist, Experimental tests on double resolution coherent imaging via STEM, Ultramicroscopy 48 (1993) 304–314.

[10] A.M. Maiden, J.M. Rodenburg, An improved ptychographical phase retrieval algorithm for diffractive imaging, Ultramicroscopy 109 (2009) 1256–1262.

[11] J.M. Rodenburg, R.H.T. Bates, The theory of super-resolution electron microscopy via Wigner-distribution deconvolution, Phil. Trans. R. Soc. Lond. A 339 (1992) 521–553.

[12] A.M. Maiden, M.J. Humphry, J.M. Rodenburg, Ptychographic transmission microscopy in three dimensions using a multi-slice approach, JOSA A. 29 (2012) 1606–1614.

[13] J.A. Johnston, Wigner distribution and FM radar signal design, IEE Proc. F 136 (1989) 81–87.

[14] R.H.T. Bates, M.J. McDonnell, Image Restoration and Reconstruction, Clarendon Press, Oxford, 1986.

[15] P.D. Nellist, J.M. Rodenburg, Beyond the conventional information limit: the relevant coherence function, Ultramicroscopy 54 (1994) 61–74.

[16] A.M. Maiden, M.J. Humphry, J.M. Rodenburg, Superresolution imaging via ptychography, JOSA A. 28 (2011) 604–612.

[17] A.M. Maiden, G.R. Morrison, B. Kaulich, A. Gianoncelli, J.M. Rodenburg, Soft X-ray spectromicroscopy using ptychography with randomly phased illumination, Nat. Commun. 4 (2013) 1669.